coatings

Article

In Situ Synthesis and Tribological Characterization of TiC–Diamond Composites: Effect of the Counterface Material on Wear Rate and Mechanism

Yuqi Chen [1,*], Jin Li [1], Liang Li [1], Ming Han [2,*] and Junbao He [1]

[1] School of Mechatronics Engineering, Nanyang Normal University, Nanyang 473061, China; liang0320@126.com (L.L.); hejunbao@nynu.edu.cn (J.H.)
[2] Henan Building Materials Research and Design Institute Co., Ltd., Henan Academy of Sciences, Zhengzhou 473061, China
* Correspondence: chenyq@nynu.edu.cn (Y.C.); daiganbing@163.com (M.H.)

Abstract: TiC bonded diamond composites were prepared from a mixture of Ti, graphite, and diamond powders as raw materials, with Si as sintering additives, through high-temperature and high-pressure (HTHP) technology. The reaction between Ti and graphite under 4.5–5 GPa pressure and 1.7–2.3 kW output power can produce TiC as the main phase. The diamond particles are surrounded by TiC, and the interface is firmly bonded. The coefficient of friction (COF) of TiC–diamond composites with POM and PP balls decreases with increasing load for a specific friction velocity. However, the COF of TiC–diamond composites with agate, Cu and Al balls increases with the rising load because of the enhanced adhesive wear effect. The COF of PP, Cu and Al balls slightly increases with the increase in friction velocity at a certain load. SEM results show that the surface of agate balls has rough, pear-shaped grooves and shallow scratches. The scratches on the surface of POM balls are wrinkled. The PP balls have pear-shaped groove scratches on their wear surfaces. The wear mechanism of TiC–diamond composites with Cu ball pairs is primarily adhesive wear. The abrasion of TiC–diamond composites with Cu ball pairs remains almost unchanged as the load increases. However, the depth and width of the pear-shaped grooves on the wear surface of TiC–diamond composites are significantly increased. This phenomenon may be attributed to the high rotational speed, which helps to remove the residual abrasive debris from the friction grooves. As a result, there is a decrease in both the depth and width of the pear-shaped grooves, leading to a smoother overall surface. The wear mechanism of TiC–diamond composites with Al ball pairs is abrasive wear, which increases with an increasing load. When the load is constant, as the speed increases, the wear morphology of TiC–diamond composites with Al ball pairs transitions from rough to smooth and then back to rough again. This phenomenon may be attributed to the wear mechanism at low speeds being groove wear and adhesive wear. As the speed increases, the wear particles are more easily removed from the wear track, leading to a reduction in abrasiveness. As the speed increases, the wear surface becomes roughened by a combination of grooves and dispersed wear debris. This can be attributed to the increased dynamic interaction between surfaces caused by higher speed, resulting in a combination of abrasive and adhesive wear. In addition, Cu and Al ball wear debris appeared as irregular particles that permeated and adhered to the surface of the TiC phase among the diamond particles. The results suggest that TiC–diamond composites are a very promising friction material.

Keywords: diamond composites; TiC; HPHT; tribological properties

check for updates

Citation: Chen, Y.; Li, J.; Li, L.; Han, M.; He, J. In Situ Synthesis and Tribological Characterization of TiC–Diamond Composites: Effect of the Counterface Material on Wear Rate and Mechanism. *Coatings* **2024**, *14*, 735. https://doi.org/10.3390/coatings14060735

Academic Editor: Cecilia Bartuli

Received: 6 May 2024
Revised: 5 June 2024
Accepted: 6 June 2024
Published: 8 June 2024

Copyright: © 2024 by the authors. Licensee MDPI, Basel, Switzerland. This article is an open access article distributed under the terms and conditions of the Creative Commons Attribution (CC BY) license (https://creativecommons.org/licenses/by/4.0/).

1. Introduction

Diamond composites with high thermal conductivity, high hardness, high modulus, and additional excellent characteristics are widely employed in aerospace, new energy-saving automobiles, abrasives, nuclear fusion, and other fields [1]. Diamond composites are made by sintering a mixture of diamond and bonding materials under HTHP [2,3].

Compared to hot press sintering (35 MPa) and discharge plasma sintering (50–80 MPa) techniques, the high temperature and high-pressure technique not only ensures diamond stability but also refines the grains. This is beneficial to the hardness and densification of diamond composites. Moreover, the structural densities of hot-pressure sintering, and discharge plasma sintering are somewhat different compared with high-temperature and high-pressure sintering. The difference in structure influences the hardness and wear resistance of the composites.

The type and content of the binder, as well as the bonding between the diamond and the binder, are important factors affecting the performance. Diamond composites require bonding materials with high hardness, close to that of diamond, high-temperature thermal stability, sinterability, a slightly higher coefficient of expansion than diamond, and the ability to form a metallurgical bond with diamond abrasive grains [4].

The Ti-Si series of bonding agents involves the sintering of Ti and Si with diamond micropowders at high temperature and pressure, during which covalent bonding compounds TiC and SiC are formed to connect the diamonds [5]. Difficulty in sintering between the bonding agent and the diamond, along with high sintering temperatures, make diamond composites less tough and more prone to brittle fracture [6]. HTHP sintering technology has the advantages of high reaction temperature, fast sintering speed, and an extremely short reaction time [7]. In our previous studies, high-purity Ti_3SiC_2 powder was synthesized through pressure-less synthesis and then mixed with diamond or cBN powder to sinter the bulks by HTHP [8–10]. Titanium–aluminum–carbon bonded cBN composites can be in situ synthesized by high-temperature and high-pressure sintering of Ti, Al, and C [11]. Cubic boron nitride (cBN)–diamond composites with Ti_3SiC_2 additive have been prepared by the HTHP process [12,13]. PcBN has been produced using Ti_3AlC_2-Al as the binder by the HTHP method [14].

Compared with ternary carbide Ti_3SiC_2 or Ti_3AlC_2, the binary carbide TiC exhibits excellent physicochemical properties, excellent thermal stability, and good wear resistance [15]. However, the high melting point and difficult sintering of TiC, as a strong covalent bonding compound, limit its application as a bonding material for diamond composites [16]. So far, there have been very few studies on TiC–diamond composites. In addition, the preparation of TiC bonded diamond composites by HTHP sintering has not been reported.

Thus, we have attempted to in situ manufacture TiC–diamond composites by HPHT, employing elemental powders to create a unique super-hard material. The COF and wear rates of the as-prepared composites with agate, Al, Cu, polyoxymethylene (POM), and polypropylene (PP) balls are discussed. We also discuss the wear mechanisms of different friction partners based on the wear morphology of TiC–diamond composite bulks and test balls. Several mechanical properties were also measured.

2. Materials and Methods

Starting powders of Ti (325 mesh, 99.3 wt. % pure, Aladdin Reagent (Shanghai) Co., Ltd., Shanghai, China), graphite (200 mesh, 99.8 wt.% pure, Henan Huaxiang Toner Technology Co., Ltd., Zhengzhou, China), and Si (325 mesh, >99.7 wt.%, Tianjin Weichen Chemical Reagent Science and Trade Co., Ltd., Tianjin, China), were employed in this research. The mixtures were combined with diamond particles (~50 μm, Xingyangshi new source chemical Co., Xingyangshi, China) in a volume ratio of 1:1. TiC–diamond samples were manufactured with an output power of 1.7–2.3 kW and a pressure of 4.5–5 GPa.

The synthesized composites were examined by XRD and SEM and the test parameters were similar to those in Refs. [17,18]. The crystal structure of the samples was analyzed by a smart X-ray diffractometer (SmartLab series, Rigaku, Japan, radiation source CuKα, voltage 40 kV, current 30 mA) with a scanning range of 10°~80°. The morphology of the products was observed using a field emission electron microscope (SEM, JSM6700F, Nippon Electron Co., Ltd., Tokyo, Japan); and the elemental compositions of the products were analyzed using an energy spectrometer (Oxford Explorer 30, Oxford Instruments, Oxford,

UK). The binding energy of chemical elements on the filler surface was determined by X-ray photoelectron spectroscopy (XPS, Thermo Scientific K-Alpha+, ThermoFisher, Waltham, MA, USA) using an Al Ka laser (λ = 0.83 nm, hν = 1486.6 eV). Friction performance test parameters and abrasion characterization were similar to those in Refs. [17,18].

3. Results

3.1. Composition of TiC–Diamond Composites

Figure 1 shows selected XRD patterns of the TiC–diamond compacts sintered under high pressure-temperature conditions. As illustrated in Figure 1, peaks of diamond and TiC are noticeable. It was proven that TiC was generated under 3.5~4.5 GPa and TiC–diamond bulks formed in situ by HPHT. The content of TiC increases following higher sintering temperatures. The newly formed TiC crystals have a strong bond with diamond. The addition of silicon does not promote the formation of Ti_3SiC_2; it is hypothesized that silicon forms a liquid phase that volatilizes at high temperatures. This is in agreement with literature reports on the destabilized decomposition of Ti_3SiC_2 under high pressure [19] and the synthesis of Ti_3SiC_2 with a non-stoichiometric ratio under 2 GPa [20]. The synthesis of SiC/TiC/diamond composites from Ti, Si and diamond powders by discharge plasma sintering has been previously reported in the literature [21]. The formation of SiC is related to the graphitization of the diamond surface during the sintering process [21]. High-temperature and high-pressure sintering avoids diamond graphitization, and graphite reacts preferentially with Ti, with no characteristic SiC peaks observed.

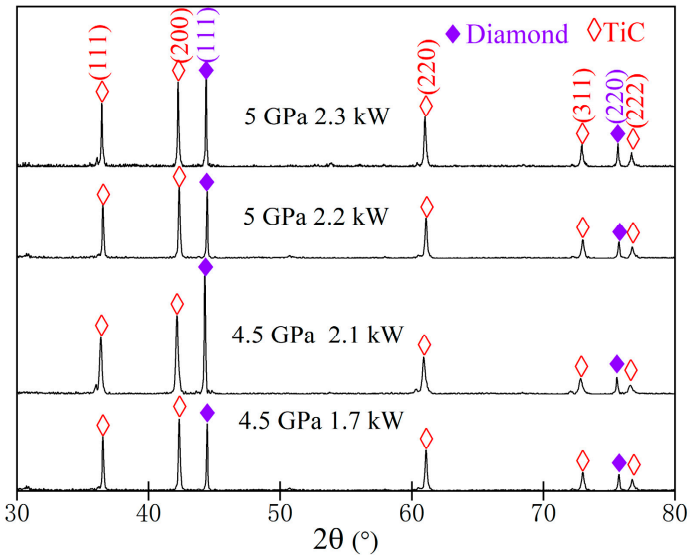


Figure 1. XRD patterns of TiC–diamond under 4.5–5 GPa.

3.2. SEM/EDS and XPS Analysis of TiC–Diamond Composites

Figure 2 shows the SEM morphology and EDS analysis of the diamond composites prepared under a sintering pressure of 4.5–5 GPa and a set output power of 1.7–2.3 kW. In the figure, the black particles represent the diamond phase, the white particles represent the amorphous phase of the binder aid Si, and the gray particles represent the TiC phase. The TiC phase was synthesized at a pressure of 4.5 GPa and an output power of 1.7 kW but the sintered sample was insufficiently microcracked (Figure 2a). The microcracks disappeared at an output power of 1.8 kW (Figure 2b). At an output power of 2.1 kW, the diamond particles were inlaid in the TiC phase and it was assumed that the diamond particles and TiC were combined by chemical bonding (Figure 2c). The microstructure of the composites becomes denser with increasing sintering pressure and temperature (Figure 2d,e). EDS analysis indicates that the Si element is present in the bonded phase.

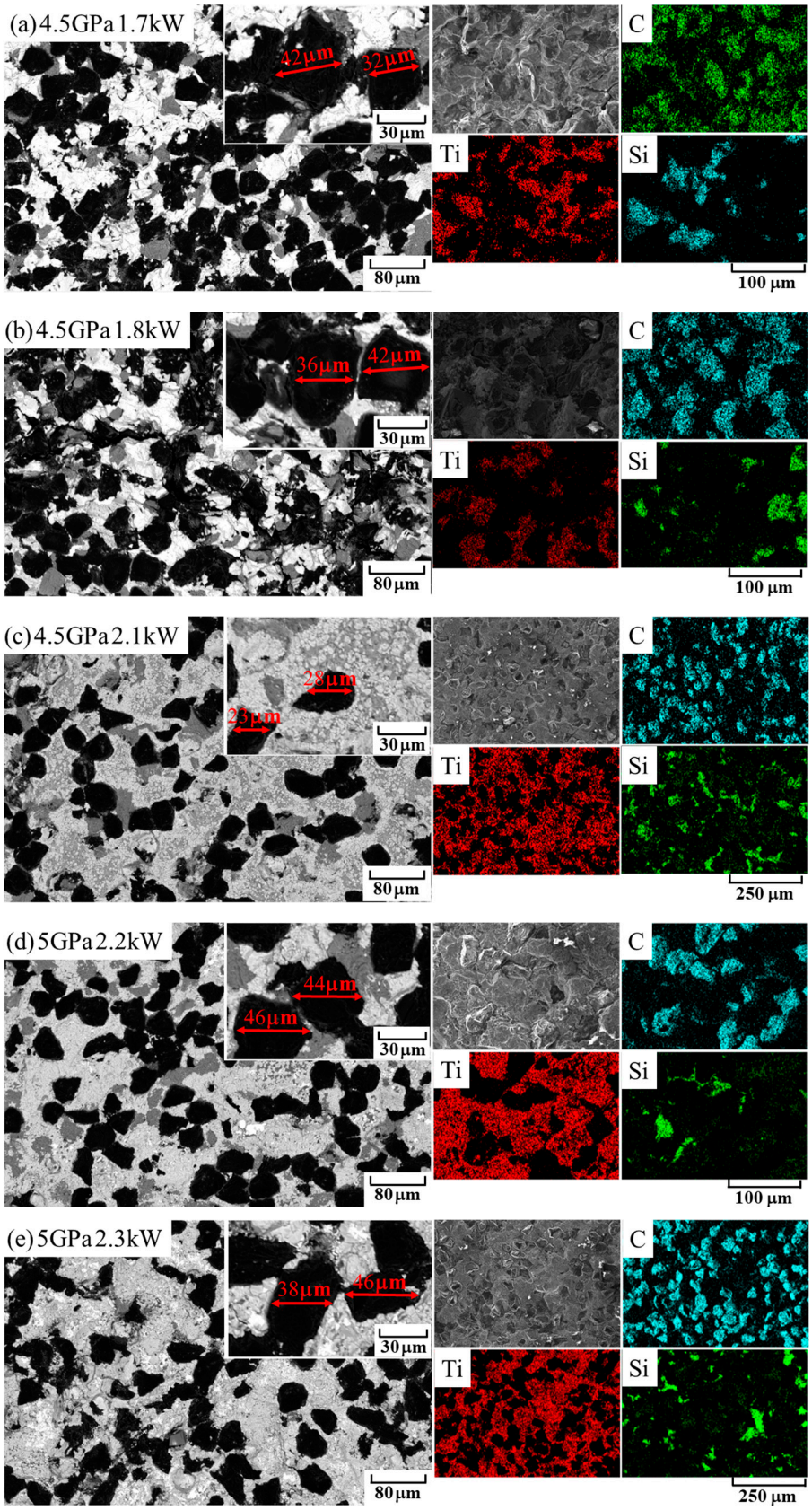


Figure 2. SEM and EDS image of TiC–diamond composites; (**a**) 4.5 GPa and 1.7 kW; (**b**) 4.5 GPa and 1.8 kW; (**c**) 4.5 GPa and 2.1 kW; (**d**) 5 GPa and 2.2 kW; (**e**) 5 GPa and 2.3 kW.

The full XPS spectrum of the sample is shown in Figure 3a and four characteristic peaks are observed at 100, 284.88, 455.5, and 531.8 eV, belonging to Si 2p, C1s, Ti 2p, and O 1s, respectively. The C1s spectrum shows a peak at 284.88 eV that is attributed to the sp3 C-C bonding in the diamonds [22,23], suggesting the presence of diamond phases in the composites. In Figure 3b, the XPS spectrum of Ti 2p can be categorized into two peaks at 455.08 and 461.68 eV that correspond to the Ti-C bonding of Ti $2p_{3/2}$ and the Ti-C bonding of Ti $2p_{1/2}$, respectively [24–26]. The XPS spectrum of Si 2p in Figure 3c is affected by the preparation process. At 1.7 kW output power, there is only a characteristic peak of the Ti–Si bond [27,28], which corresponds to the characteristic peak of Si in Ti_3SiC_2 at 99.5 eV, indicating the existence of a small amount of Ti_3SiC_2. With the increase in output power to 1.8 kW, the characteristic peak of Si 2p becomes two and the characteristic peak at 102.3 eV corresponds to that of Si^{4+} $2p_{2/3}$ in SiO_2 [29,30], which indicates the detachment of the atomic layer from Ti_3SiC_2 and the oxidation of the Ti $2p_{1/2}$ Ti-C bond. It is assumed that the atomic layer of Si in Ti_3SiC_2 escapes and oxidizes to form SiO_2 at the same time. The characteristic peak at 285 eV in Figure 3d corresponds to the characteristic peak of diamond and there is a characteristic peak of Ti-C [31].

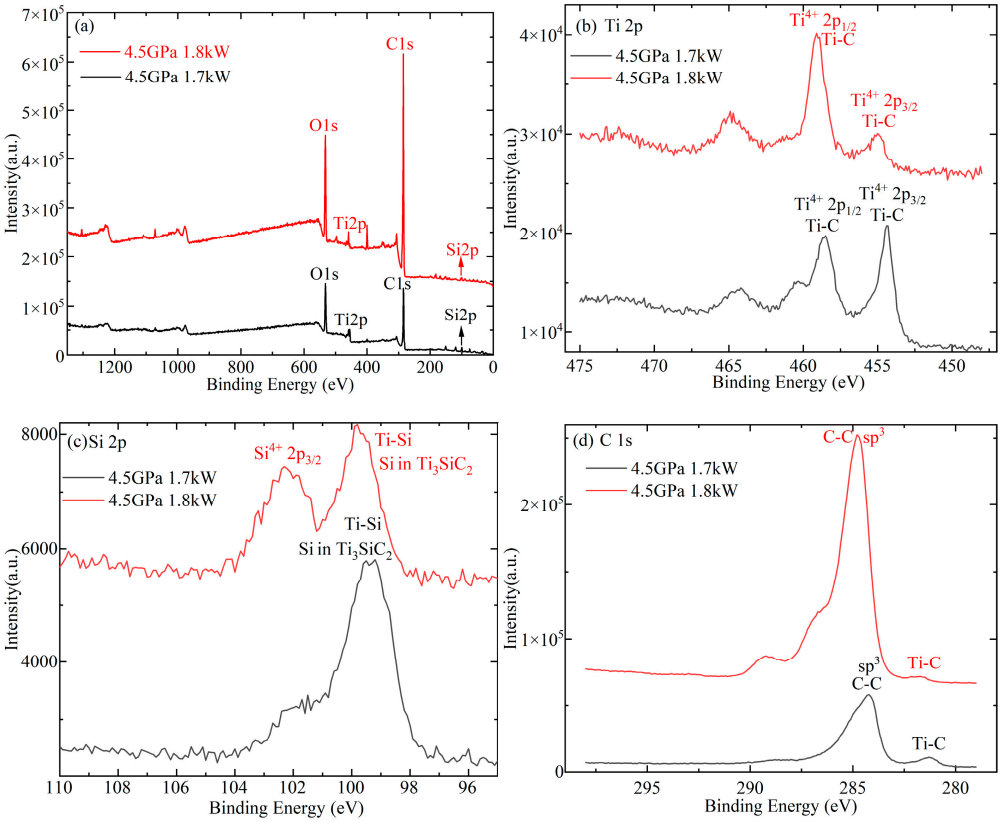


Figure 3. XPS spectroscopy of TiC–diamond composite (**a**); High-resolution spectra of Ti peaks (**b**); Si peaks (**c**); C peaks (**d**).

3.3. Friction Properties of TiC–Diamond Composites

3.3.1. Agate

Figure 4a shows the COF of TiC–diamond composites with an agate pair under different loads. The COF is small and the average value is about 0.11 at low load (5 N). As the load increases, the COF initially rises and then reduces. The average COF increases to 0.236, 0.295, and 0.285 at loads of 8 N, 10 N, and 12 N, respectively. This increase is attributed to the diamond superhard particles and the agate dyads, which are high-hardness materials. The abrasive wear effect remains almost unchanged during the friction process. The increase in the COF is mainly due to the enhancement of the adhesive wear effect (Figure 4b), indicating that the load mainly affects the adhesive wear in TiC–diamond and

agate pairings. The COF of TiC–diamond composites with agate is significantly smaller than that of TiC-Ti_3AlC_2 or TiC-Ti_2AlC (0.8~1, under 12 N at 300 rpm/min) [17].

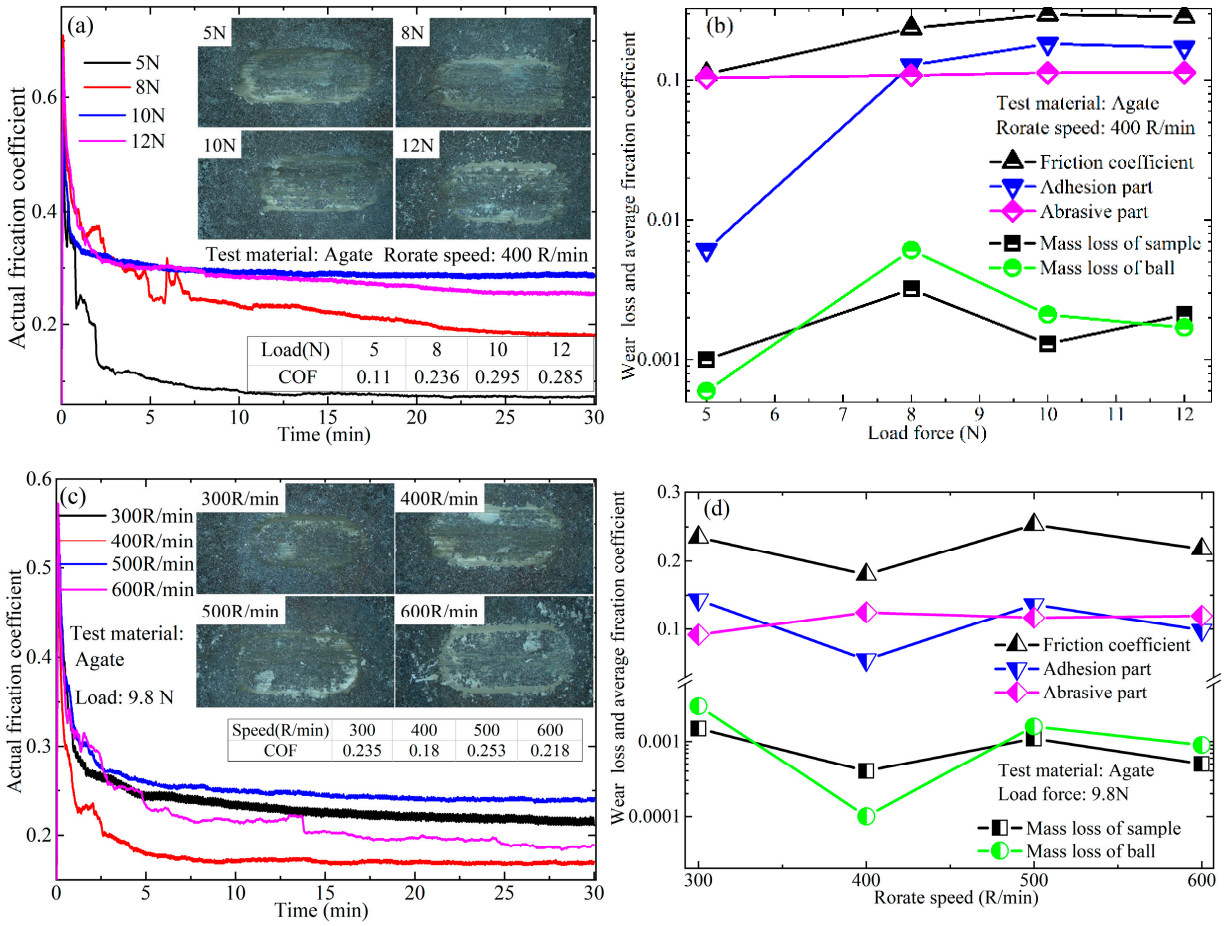


Figure 4. COF (**a**) and abrasion loss (**b**) of synthetics with agate pair under 5 −12 N at 400 rpm/min; COF (**c**) and abrasion loss (**d**) of synthetics under 9.8 N at 300 −600 rpm/min.

Figure 4c shows the variation of COF with rotational speed of TiC bonded diamond composite material at 9.8 N against agate ball. As the rotational speed increases, the COF shows a fluctuating pattern of firstly decreasing and then increasing and then decreasing. The COF reaches its minimum value at 400 rpm/min, which is 23.45% lower than that at 300 rpm/min. Then the COF increases and stabilizes at 500 rpm/min, and the fluctuation of the COF with the change of test time is not big. The reason for the variation of COF is the fluctuation of adhesive wear with the increase in rotational speed (Figure 4d). The COF of Ti_2AlC–TiC and Ti_3AlC_2–TiC composites and the agate ball counterpart varies with sintering pressure and the average COF fluctuates between 0.5 and 1.2 [17].

Figure 5 shows an SEM image of the wear track of TiC–diamond composites with an agate ball under 8 N at 400 rpm/min. The black diamond particles were encapsulated by the bonding phase, and no pits formed by diamond spalling were observed. The TiC bonding phase was synthesized by an in situ chemical reaction of Ti elemental powder under high pressure to improve the wettability of the diamond surface. The gray color represents the bonding phase of TiC. The white agate ball abrasive chips adhered to the surface of the wear marks, indicating that severe adhesive wear occurred on the contact surfaces. There are no obvious groove scratches on the surface of the abrasion marks, indicating that the high temperature formed during the friction process between TiC–diamond composites and agate exhibits certain anti-wear and friction reduction properties.

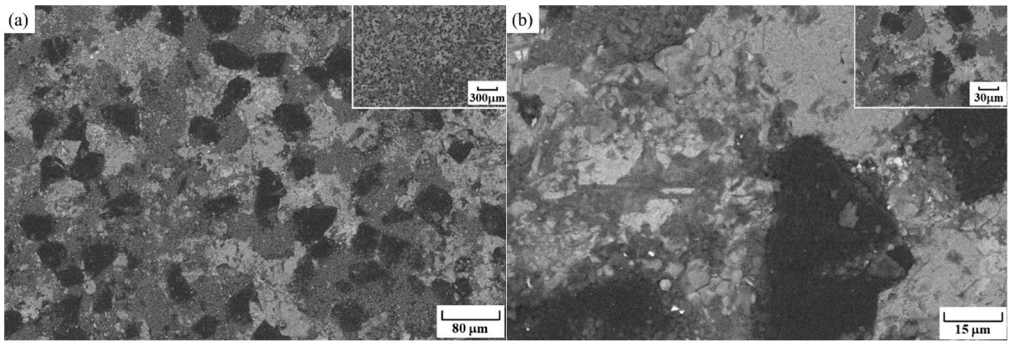


Figure 5. SEM image of wear track of synthetics; X200 (**a**), local zoom in X1000 (**b**).

Figure 6a–d shows SEM images of the wear track of agate balls tested at 400 rpm/min under 5–12 N. Combined with SEM at low magnification, the wear surfaces of the agate balls consist of shallow furrows, and a small amount of flaking abrasive debris is gradually generated with an increase in load.

Figure 6e–h displays SEM images of the wear track of an agate ball under a load of 9.8 N at 300–600 rpm/min. The microscopic morphology of the samples with the change of rotational speed is basically the same, and parallel to the sliding direction of the pear groove and flaking pits. The surface abrasion is more serious and black abrasive particles with smaller sizes are retained in the flaking pits (Figure 6e). These granular abrasive particles play the role of abrasive in the friction process, exacerbating the wear of the friction sub-surface.

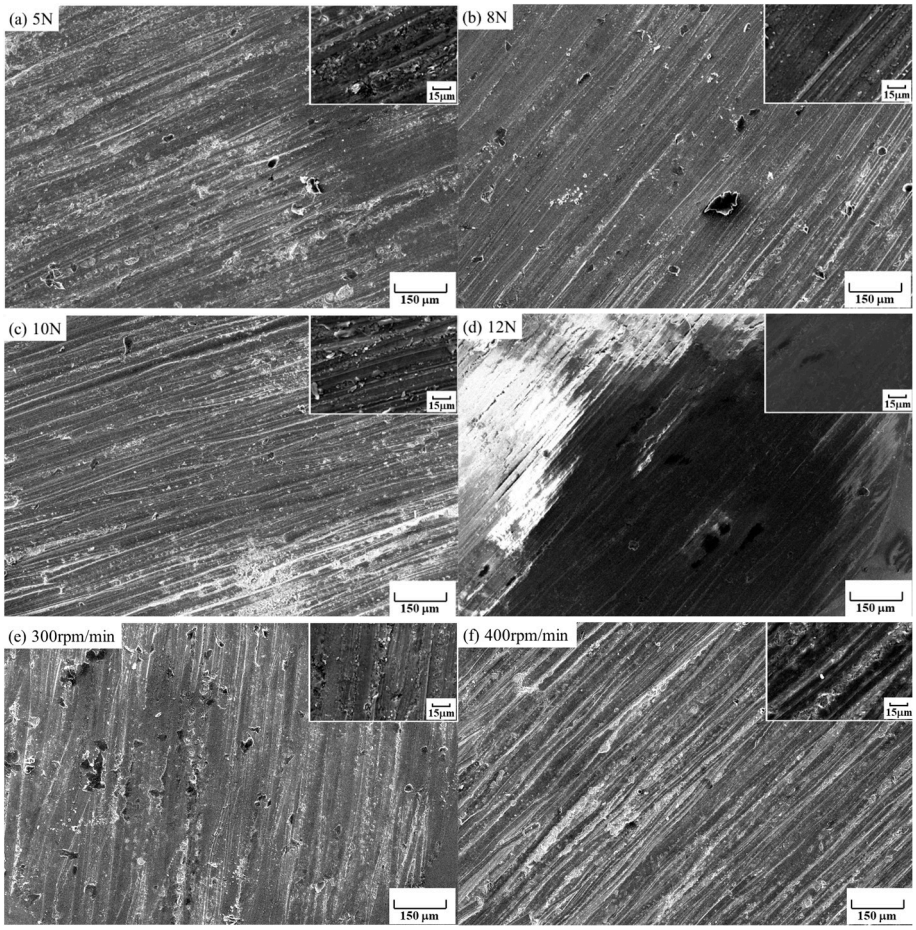


Figure 6. *Cont.*

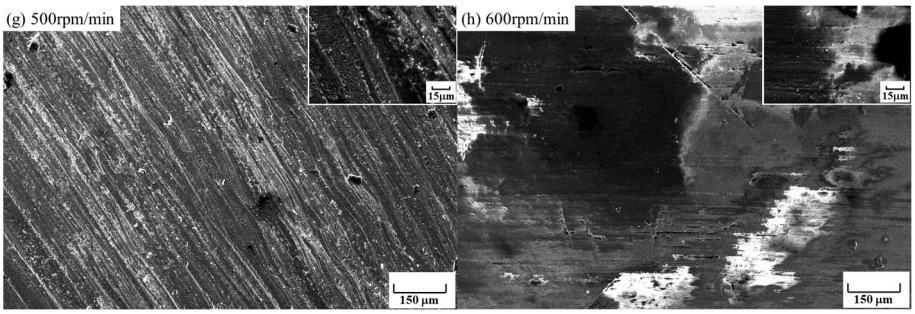


Figure 6. SEM image of wear track of agate ball under 5 N (**a**); 8 N (**b**); 10 N (**c**); 12 N (**d**) at 400 rpm/min; under 9.8 N at 300 rpm/min (**e**); 400 rpm/min (**f**); 500 rpm/min (**g**); 600 rpm/min (**h**).

3.3.2. POM

Figure 7a shows the curves of COF of TiC–diamond composites and POM pairs over time under different loads. Observing the time–COF curves, the friction experiments can be divided into three phases: the first phase, roughly from 0 to 5 min, is the break-in phase, during which the curves oscillate violently. In the second stage, from 5 min to 22 min, the curve tends to stabilize and begin to show a gradual decline, which may be due to the increasing abrasion marks during the friction process increasing the contact area so that the COF can gradually reduce. During the third stage, which lasts from 22 min until the end of the experiment, the COF is maintained near the low value and some experimental groups are accompanied by large fluctuations in which the lubricant film realizes the dynamic balance between fragmentation and generation, and the speed of abrasion mark increase slows down. When the test load is 8 N, the COF is lower at the beginning of the first stage it can fall to its lowest value of the COF faster in the second stage, the stability is better in the third stage, and there is no large fluctuation phenomenon.

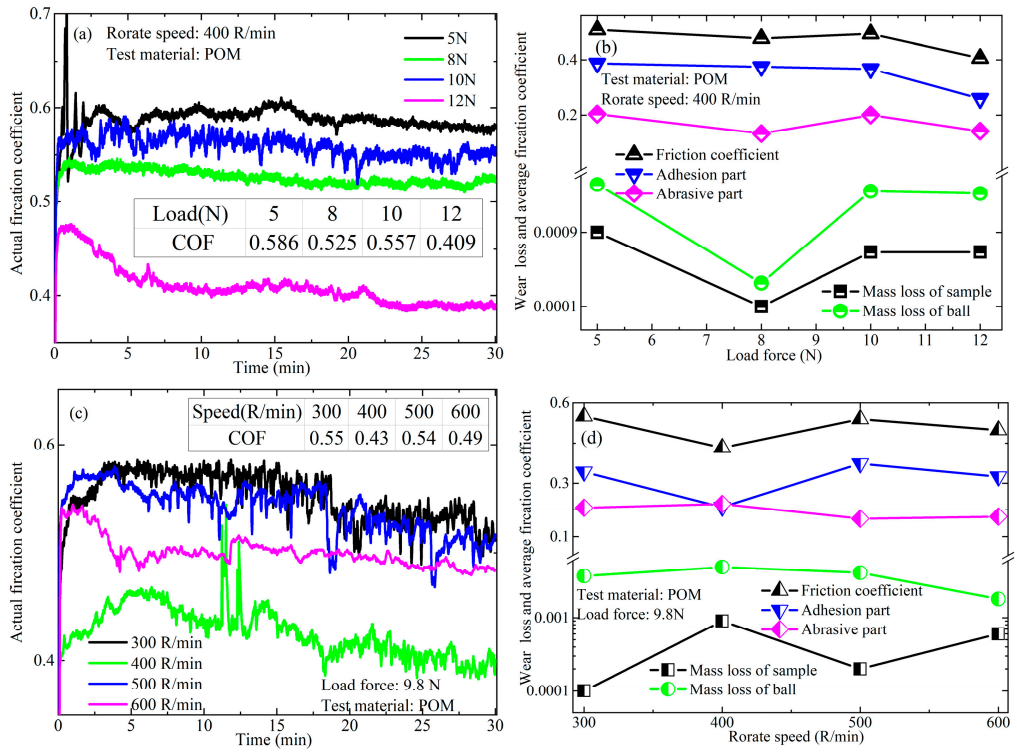


Figure 7. COF (**a**) and abrasion loss (**b**) of synthetics with POM pair under 5–12 N at 400 rpm/min; COF (**c**) and abrasion loss (**d**) of synthetics under 9.8 N at 300–600 rpm/min.

Overall, the COF is largest at 5 N, with an average COF of about 0.586. The COF of the experimental group with increased load shows an overall decrease: the decreases are 10.35%, 4.89%, and 30.18% for 8 N, 10 N, and 12 N, respectively. The mass losses showed a decrease and then an increase with increased load; the least mass losses were observed at 8 N (Figure 7b). The wear of TiC–diamond and POM is mainly adhesive wear accompanied by pear groove wear. As the load increases, the adhesive wear decreases gradually, especially at a load of 12 N, and the decrease of adhesive wear is significant. The effect of load was similar for the COF between agate and steel [32]. The reduction of the COF for POM/Al_2O_3 nanocomposites is advantageous when the load is increased [33].

As shown in Figure 7c, the COF first falls and subsequently increases as the rotational speed rises. The magnitude of change of the COF is relatively small for 300 rpm/min and 500 rpm/min rotational speeds, and the COF decreases and has a larger magnitude for the 400 rpm/min rotational speed. This is comparable to the POM/steel COF fluctuation rule with rotational speed [32]. The COF of POM parallel line gear pairs varies between 0.35 and 0.45 [34]. Combined with the relatively small change in abrasive wear with increasing rotational speed shown in Figure 7d, the role of adhesive wear is significantly reduced at 400 rpm/min. The TiC–diamond specimen has the largest mass loss at 400 rpm/min. The COF of Ti_2AlC–TiC and Ti_3AlC_2–TiC composites and POM pairs fluctuates between 0.17 and 0.37 [17], which is lower than that of TiC–diamond composites. The average COF of $Ti_3Si_{0.8}Al_{0.2}C_2$–diamond composites and POM pairs is between 0.42 and 0.65, which is similar to that of TiC–diamond composites [18].

Figure 8a shows SEM images of the wear track of TiC–diamond composites with a POM pair. The abrasive debris from POM balls mainly adheres to the TiC surface and these abrasive particles are bonded to each other in the form of flakes. Figure 8b–e shows the SEM images of the wear marks on the end face of the POM ball under different loads. There are many fish scale-like micro bumps on the surface of the POM ball, which is a typical manifestation of adhesive wear. Abrasive debris is an important information carrier and evidence of the wear mechanism in the friction wear process. The abrasive chip patterns generated after wear are marked with circles. Abrasive chip morphology on the main body was flaky; it is generally believed that flaky abrasive chips are caused by the pressure between the grinding surface of the abrasive chip, which was crushed and ironed out, and the product of the abrasive wear mechanism is mainly for the adhesive wear, which is consistent with the large area of the surface of the specimen from the phenomenon of the transfer of the material adhesion to the conclusions drawn.

Figure 8b–d shows the morphology of the abrasion marks under the conditions of 5 N–10 N; the pear grooves in the abrasion marks under these conditions are obviously deepened, and the amount of abrasive chips in the pear grooves is obviously increased. Changes in the pear groove are easier to observe in optical abrasion photographs. Optical photographs of POM ball abrasion marks were shown in Figure S1. The abrasive chips adhering to the edge of the pear groove are in the form of strips, which is a more obvious characteristic of cutting wear abrasive chips. The cutting wear particles are formed by hard and sharp micro-convex bodies (hard phase diamond particles) plowing on the softer and lower hardness POM wear surface. Here, it is demonstrated from the point of view of wear mark morphology and chip morphology that more severe plowing and even cutting wear effects do occur under different loading parameters. Figure 8e shows the chip morphology under the optimal wear reduction load condition (12 N), demonstrating that the chip particle size is reduced compared to other load conditions, the chip morphology tends to be irregular lumps, and there are very few large particle sized flakes. This suggests that an appropriate increase in load effectively reduces the large-area adhesive transfer of the material during the abrasion process.

Figure 8f–h shows SEM photographs of the surface morphology of the abraded area of the POM balls at different rotational speeds. The morphology of the wear marks at 300 rpm/min and 500 rpm/min is similar to the results shown in Figure 8b–e, while the

pear groove in the morphology of the wear marks at 400 rpm/min is obviously deepened, which indicates that the abrasive wear effect is enhanced.

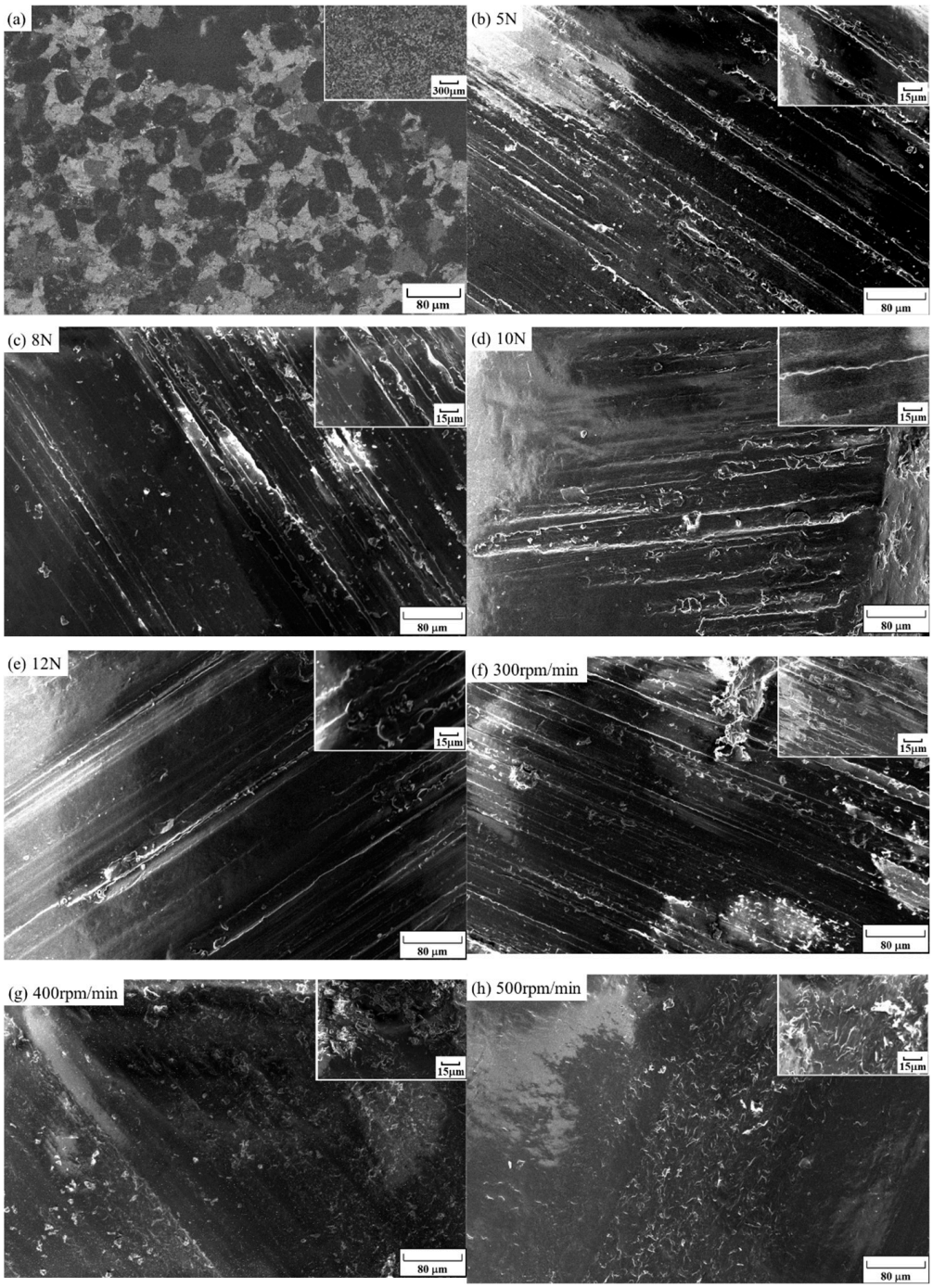


Figure 8. SEM image of wear track of synthetics (**a**); POM ball under 5 N (**b**); 8 N (**c**); 10 N (**d**); 12 N (**e**) at 400 rpm/min; under 9.8 N at 300 rpm/min (**f**); 400 rpm/min (**g**); 500 rpm/min (**h**).

3.3.3. PP

Figure 9 shows the COF and mass loss of the TiC–diamond and PP paired pair. The COF decreases gradually with increasing load. At a low load (5 N), there is a large fluctuation in the COF. The tribological characteristics of polypropylene (PP) are significantly influenced by its surface temperature because thermal softening can lead to an increase in wear severity [35]. When the load is increased to 8 N–12 N, the change of COF is small, and it stabilizes quickly. The tribological properties of PP-based composites filled with

nanodiamond soot particles gradually increase with increasing loads [36]. In contrast to the COF of TiC–diamond composites (0.5–0.7), the COF of Ti_2AlC–TiC and Ti_3AlC_2–TiC composites and PP pairings varies between 0.38 and 0.44 [17]. In comparison to the COF of TiC–diamond composites, the average COF of $Ti_3Si_{0.8}Al_{0.2}C_2$–diamond and PP pairings is less, ranging from 0.5 to 0.65 under 9.8 N [18].

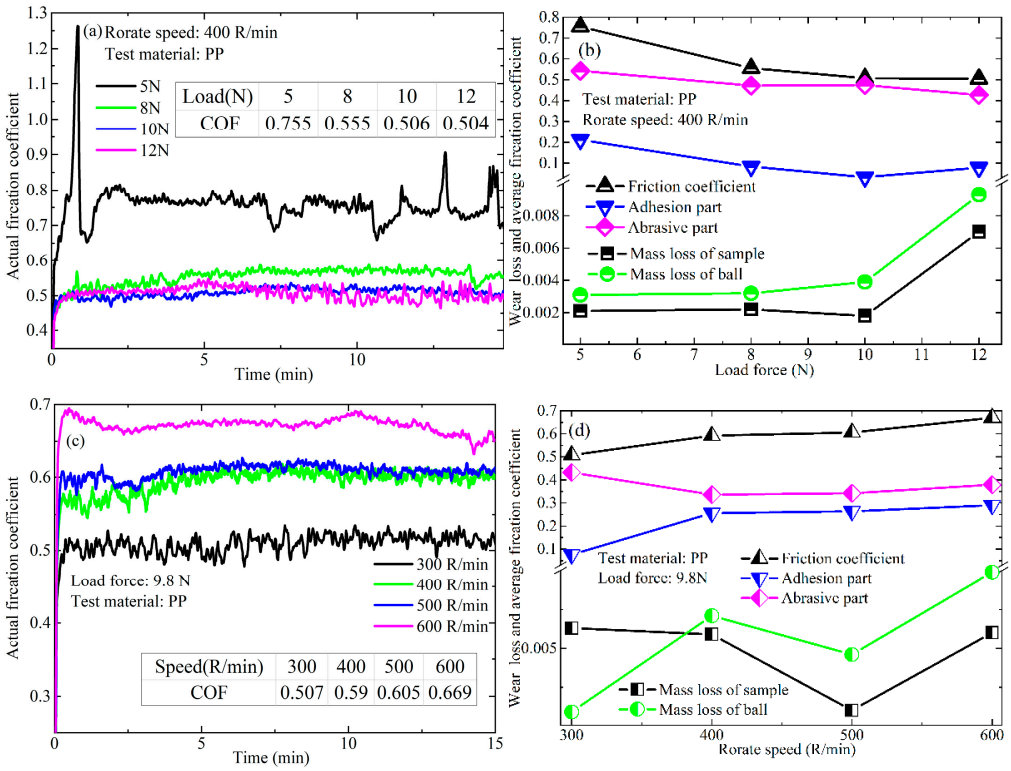


Figure 9. COF (**a**) and abrasion loss (**b**) of synthetics with PP pair under 5–12 N at 400 rpm/min; COF (**c**) and abrasion loss (**d**) of synthetics under 9.8 N at 300–600 rpm/min.

Abrasive wear accounts for the main component in the wear mechanism of TiC–diamond and PP pairs, and abrasive wear is less affected by the change of load. Load change mainly affects the adhesive wear. Adhesive wear decreases monotonically with increasing load. The mass loss of test blocks and PP balls increases with the increasing load (Figure 9b).

The effect of rotational speed on the friction characteristics of a TiC–diamond and PP paired pair is shown in Figure 9c. As the rotational speed increases from 300 rpm/min to 600 rpm/min, the average COF increases from 0.5 to 0.67. This is comparable to the COF of PP composites that have been altered with carbon nanotubes [37]. At low rotational speed (300 rpm/min), the wear mechanism is dominated by abrasive wear, accompanied by a small amount of adhesive wear. As the rotational speed increases to 400 rpm/min, the role of abrasive wear in the wear loss mechanism decreases, while the contribution of adhesive wear increases. The mass loss of the test block reaches a minimum value of about 0.001 g at 500 rpm/min. The mass loss of the PP balls shows a tendency of increasing initially, then decreasing, and increasing again with the increase of rotational speed.

Figure 10 shows SEM images of the wear track of TiC–diamond composites with a PP pair. Similar to the POM wear process, the abrasive chips from the PP balls adhere to the surface of the TiC–diamond composite.

Figure 11 shows SEM images of the abrasion marks on the end face of the PP ball under different loads. There are abrasion marks present on the surface of the specimen after friction and a lot of flaky material. The abrasion marks are caused by the rough surface of the friction sub-surface, and the flaky material is the abrasion debris that is not rubbed down after the specimen is connected to the original specimen through friction. Deep abrasion marks and some furrows exist on the surface of the specimen after friction, as

shown in Figure 11a–c, accompanied by rolls of flaky debris. The rolled debris will be dislodged in subsequent repeated friction, resulting in an increase in the amount of wear on the specimen. Figure 11d shows that, in the wear surface, furrows have become shallow, there is obviously much less rolled flaky debris and flaky debris, and the wear surface is smoother.

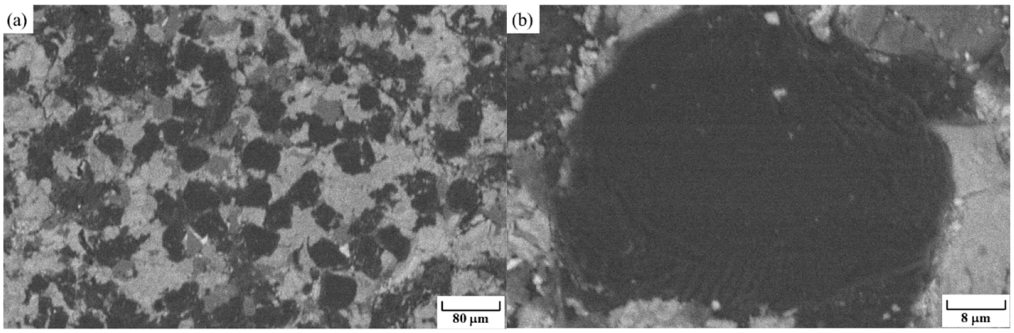


Figure 10. SEM image of wear track of the synthetics; X200 (**a**), local zoom in X2000 (**b**).

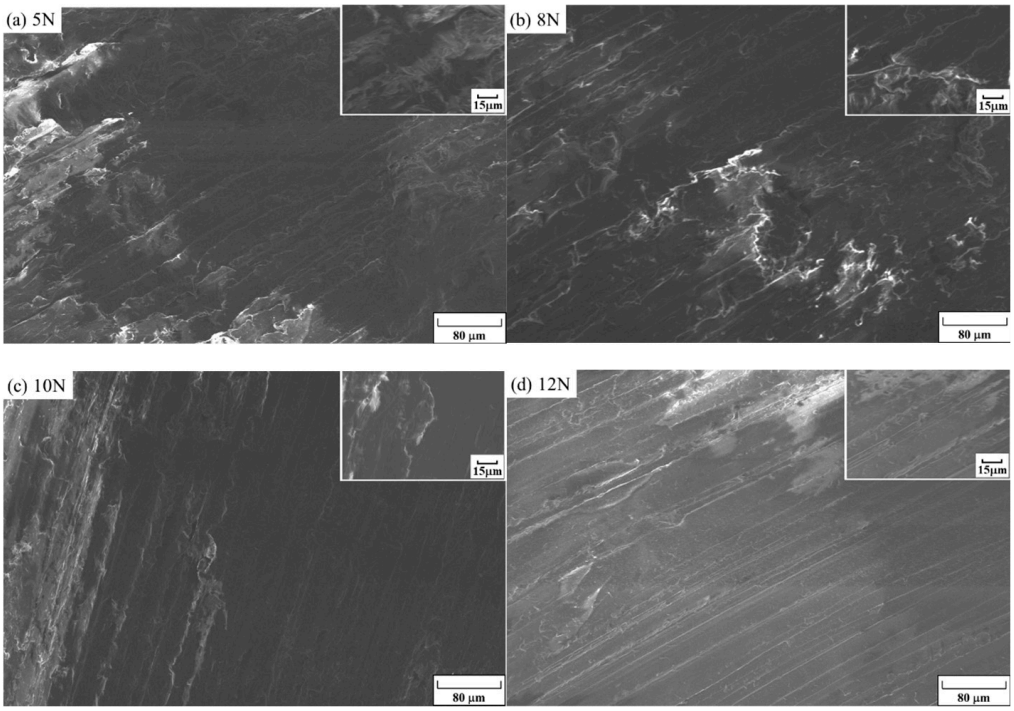


Figure 11. SEM image of wear track of PP ball under 5 N (**a**); 8 N (**b**); 10 N (**c**); 12 N (**d**).

The abraded surface of the specimen is characterized by significant adhesive detachment caused by plastic deformation, which is characterized by adhesive wear (Figure 12a). In the case of the composite material samples, not only was there significant ploughing of the wear surface, but there was also significant adhesive detachment. This characteristic increases with increasing speed (Figure 12b,c). The wear surfaces of the composite material samples showed only slight ploughing and a small amount of adhesive loss, with the wear patterns being mainly grit and adhesive wear. Grit wear and adhesive loss also increased with increasing speed (Figure 12d).

3.3.4. Cu

Figure 13a shows the COF of TiC–diamond composites with a Cu pair. The COF of TiC composites with Cu pairing at 400 rpm/min under 5 N is 0.45–0.55. The average COF of diamond/Cu composites is about 0.55 under a load of 6 N [2]. The COF increases to 0.7 with

the increase of load up to 8 N. This is mainly because the adhesive wear with the increase of load increases substantially. As the load continues to increase, the COF decreases during the run-in period and the stability gradually increases. The COF first drops before rising, which shows that the composite material has a certain load carrying capacity. The COF of TiC–diamond composites is less than that of Ti_2AlC–TiC and Ti_3AlC_2–TiC composites and Cu pairings, ranging between 0.38 and 0.77 [17]. Under 9.8 N, the average COF of $Ti_3Si_{0.8}Al_{0.2}C_2$–diamond composites and Cu pairings ranges from 0.4 to 0.55, which is comparable to that of TiC–diamond composites [18].

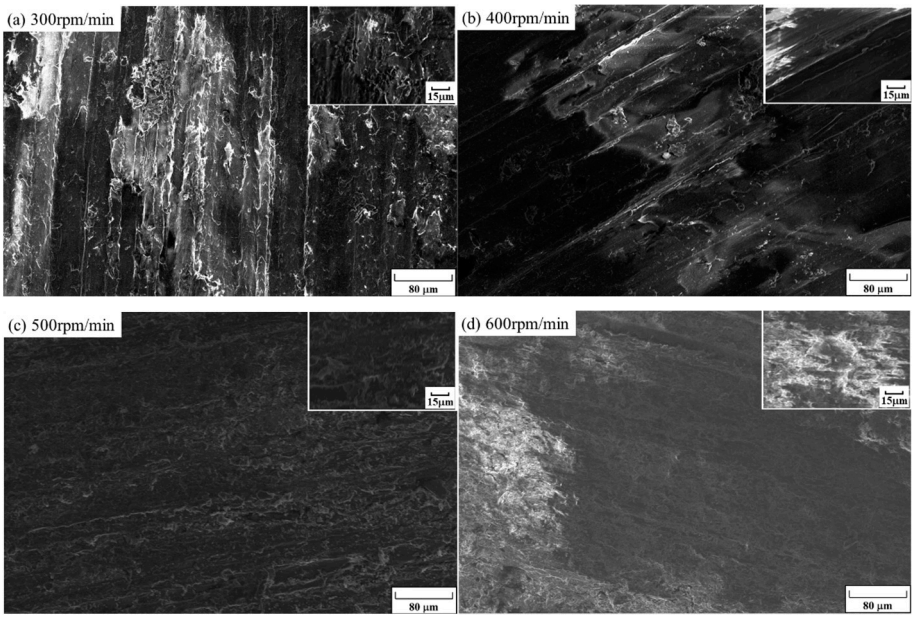


Figure 12. SEM image of the wear track of the PP ball at 300 rpm/min (**a**); 400 rpm/min (**b**); 500 rpm/min (**c**); 600 rpm/min (**d**).

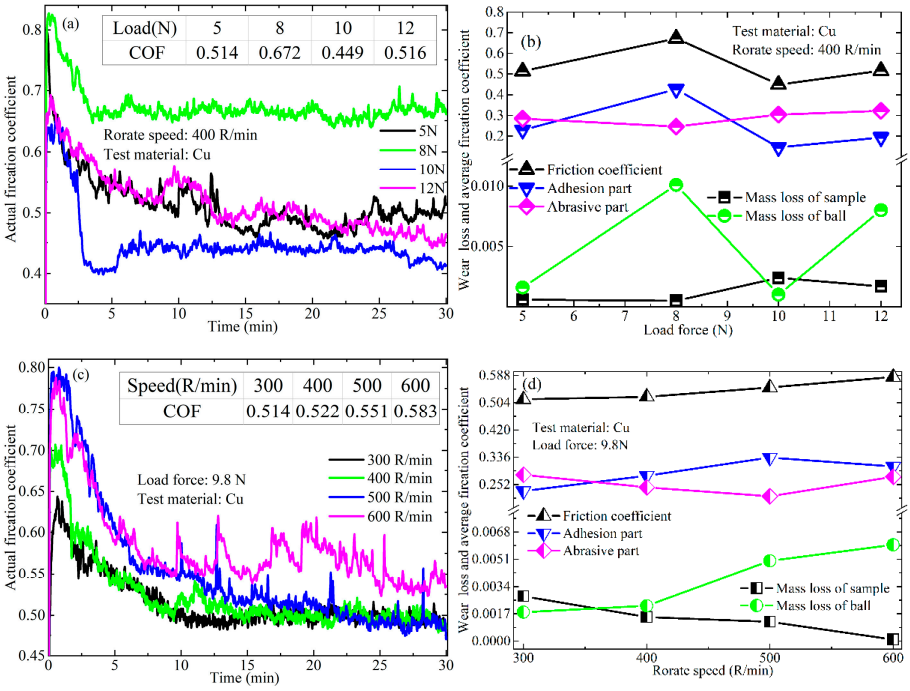


Figure 13. COF (**a**) and abrasion loss (**b**) of synthetics with Cu pair under 5–12 N; COF (**c**) and abrasion loss (**d**) of synthetics at 300–600 rpm/min.

The effect of load variation on the mass loss of the composites was relatively small with increasing load, but the mass loss of Cu balls increased significantly (Figure 13b). The adhesive wear portion of the abrasion fluctuates with increasing load. The role of abrasive wear increases slowly with increasing load. The effect of load on the COF is a result of the mutual coupling of adhesive wear and abrasive wear.

The abrasion loss of the composites varied between 0.1 and 2.8 mg (Figure 13d). The abrasion loss of the synthetics decreased with an increase in rotational speed and was maximal at 300 rpm/min, which was mostly connected to abrasive wear. The abrasion loss of the Cu balls ranged between 1.8 and 6 mg. The mass loss increased with an increase in rotational speed. The composites showed better wear resistance at higher speeds.

Figure 14 shows an SEM image of the wear track of TiC–diamond composites with a Cu pair. There were no obvious scratches on the surface of the TiC–diamond composites, and no diamond detachment was observed. The Cu ball abrasive chips appeared in the form of irregular particles, which filled and bonded to the surface of the TiC phase between the diamond particles. The EDS analysis shows that oxidation of the Cu chips occurs due to the friction temperature during the friction process.

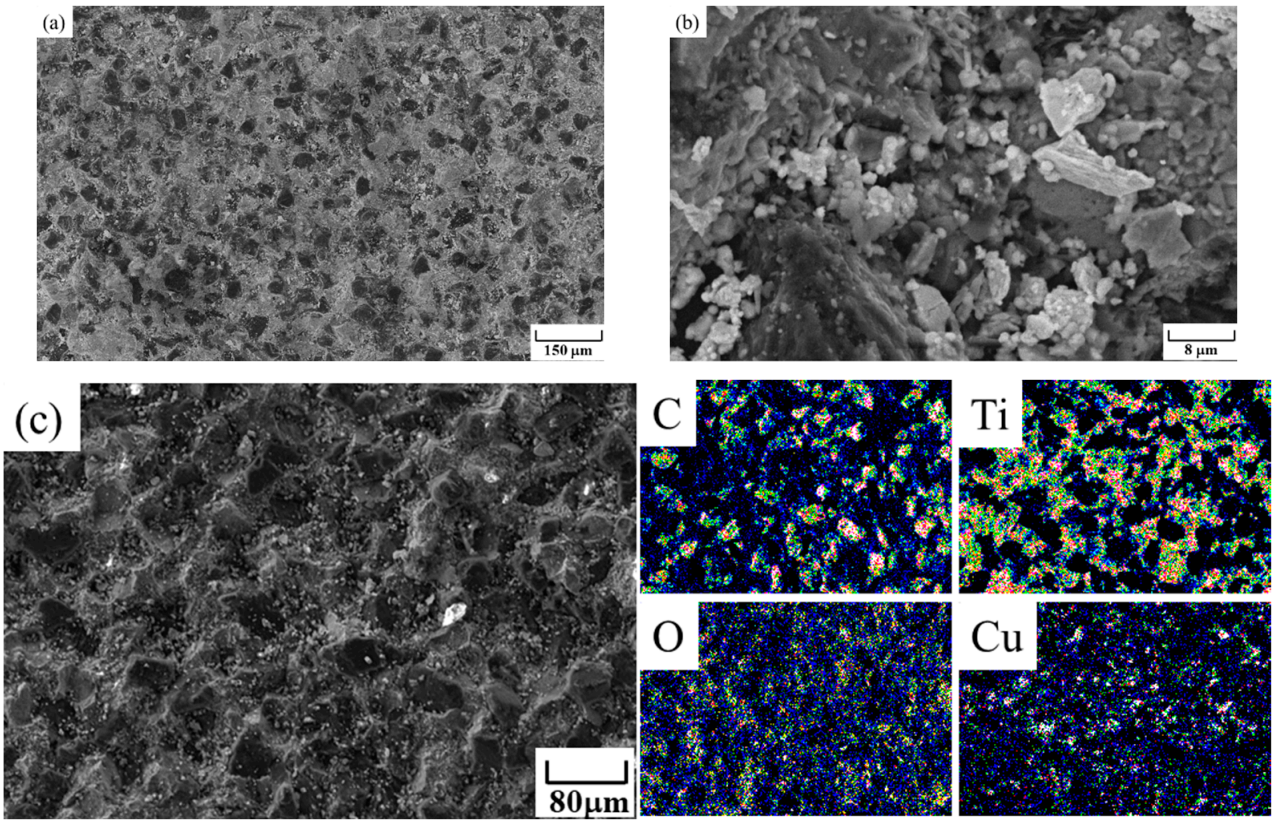


Figure 14. SEM image of the wear track of TiC–diamond composites with Cu pair; (**a**) overall shape; (**b**) localized enlargement of abrasive chips; (**c**) EDS analysis.

At a lower load (5 N), the wear is less severe. The wear surface has relatively shallow grooves and some debris accumulation (Figure 15a). The inset shows minor surface damage and some material transfer or plowing. The depth and width of the wear grooves on the pear surface increased significantly with increasing load, indicating more pronounced wear of the Cu balls (Figure 15b). There was also more visible debris. The inset shows a rougher surface texture, indicating more intense wear. The response of the material to the applied stress is nonlinear, with higher loads resulting in greater wear. The Cu balls were severely worn when the load reached 12 N (Figure 15d).

There are parallel grooves on the wear surface and many Cu chips along the wear path (Figure 15e). The enlarged image shows that large particles of wear chips are embedded

in the wear surface. Compared to the wear surface at 300 rpm/min, the wear surface at 400 rpm/min showed a decrease in debris and an increase in the adhesive wear effect (Figure 15f). As the rotational speed increases, the amount of abrasive debris decreases and the pear grooves become shallower but there are pits formed by adhesive wear (Figure 15g, magnified view). This indicates that high rotational speed generates more frictional heat, elevating the contact interface temperature, and the adhesive wear effect is enhanced. The grooves on the wear surface at 600 rpm/min become thinner, and the whole becomes smooth (Figure 15h). It is hypothesized that the high rotational speed carries residual abrasive debris out of the friction grooves and the loss of mass of the ball is large, resulting in a smooth wear surface.

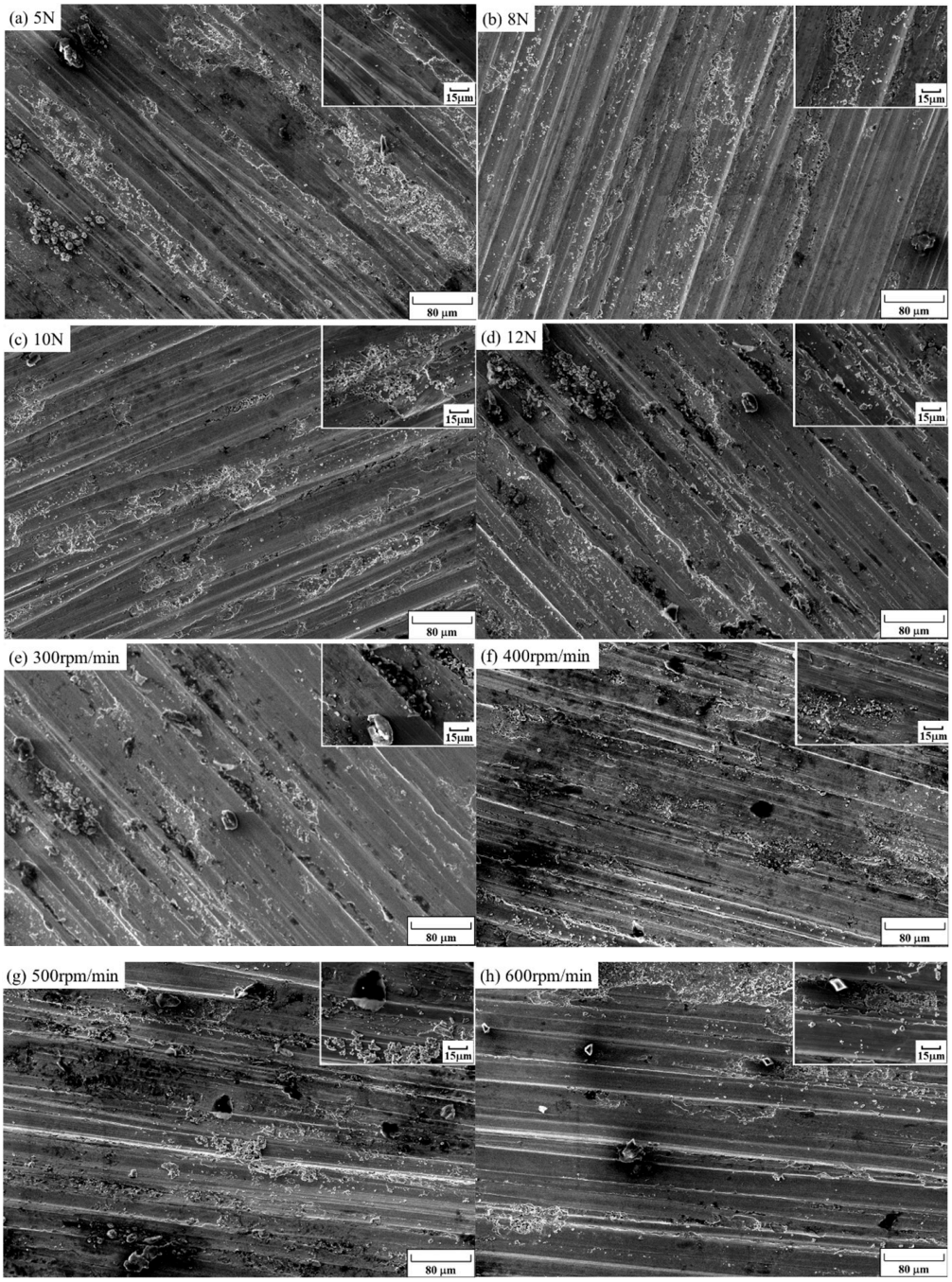


Figure 15. SEM image of the wear track of Cu ball under 5 N (**a**); 8 N (**b**); 10 N (**c**); 12 N (**d**) at 400 rpm/min; under 9.8 N at 300 rpm/min (**e**); 400 rpm/min (**f**); 500 rpm/min (**g**); 600 rpm/min (**h**).

3.3.5. Al

Figure 16a,c show the COF of TiC–diamond composites with Al pairs at different loads and rotational speeds. Overall, the load and rotational speed have a small effect on the COF. The COF is between 0.4 and 0.5. There were fluctuations in the COF with an increase in time during the test. Although the variation of COF with load increase is small, the load variation has a significant effect on the wear mechanism of TiC–diamond composites with Al paired. With the increase of load and rotational speed, the abrasive wear effect is enhanced while the adhesive wear effect is weakened (Figure 16b,d). The mass loss of test blocks and balls was small. The COF of Ti_2AlC–TiC and Ti_3AlC_2–TiC composites and Al pairs fluctuates between 0.5 and 0.8, which is larger than that of TiC–diamond composites (0.4–0.5) [17]. The average COF of $Ti_3Si_{0.8}Al_{0.2}C_2$–diamond composites and Cu pairs is between 0.5 and 0.8 under 9.8 N, which is larger than that of TiC–diamond composites [18].

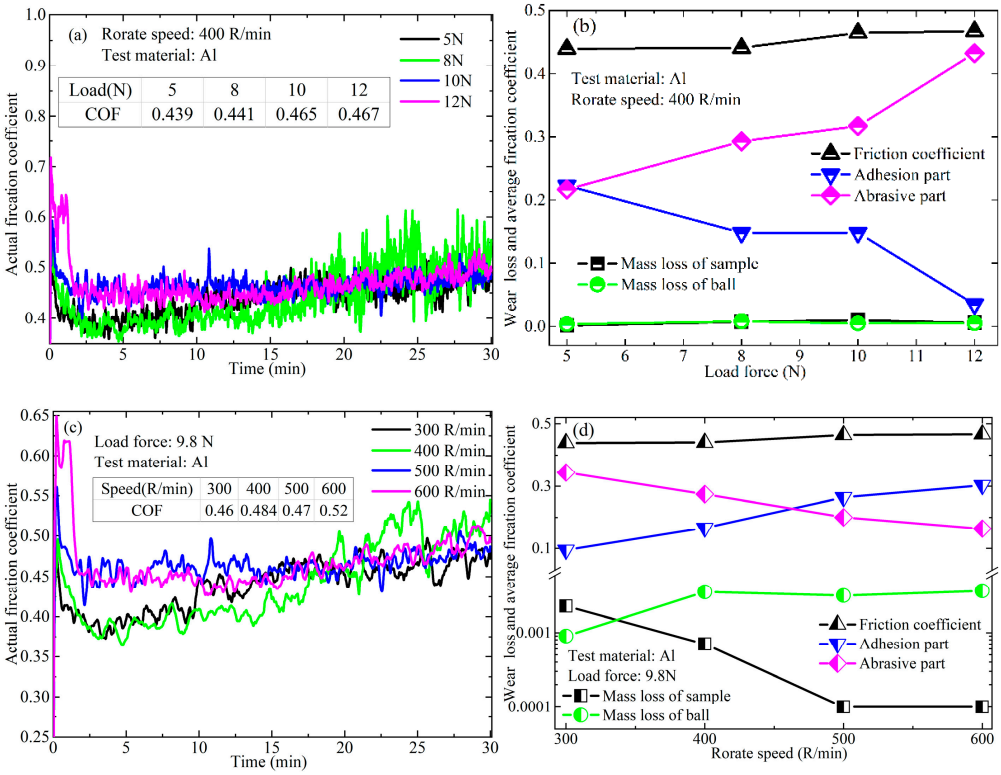


Figure 16. COF (**a**) and abrasion loss (**b**) of synthetics with Al pair under 5 −12 N; COF (**c**) and abrasion loss (**d**) of synthetics at 300 −600 rpm/min.

Figure 17a shows SEM images of the wear surface of TiC–diamond composites. Similar to the Cu wear process, the Al ball abrasive debris adheres to the wear surface and the shape of the abrasive debris is irregular. The wear surface at 5 N has grooves and a small amount of debris, indicating that the wear mechanism is a combination of pear gouge wear and adhesive wear (Figure 17b). At 8 N, the degree of adhesion to the wear surface decreases. When the load was increased to 10 N, the number of abrasive chips increased, indicating an increase in abrasive wear action. The protruding corners and large amounts of wear debris can lead to the formation of plastic deformation on the wear surface at a load of 12 N (Figure 17d).

At 300 rpm/min, the wear morphology exhibited obvious visible furrows (Figure 17e). The wear mechanism is dominated by furrow wear, accompanied by adhesive wear. The signs of surface damage and deformation can be seen in the insets. Compared with 300 rpm/min, increasing the rotational speed to 400 rpm/min can smooth the wear surface. At this speed, wear particles are more easily removed from the wear track, thus reducing abrasiveness (Figure 17f). At 500 rpm/min, the wear surface became rough,

with a mixture of grooves and scattered wear debris (Figure 17g). This may be due to the increased dynamic interaction between the surfaces caused by the increase in rotational speed, which leads to the mixing of abrasive and adhesive wear. The wear morphology at 600 rpm/min (Figure 17h) is extremely irregular with severe abrasions. This may be due to wear mechanisms such as higher interaction energy due to high rotational speed, increased temperature and stress, and increased oxidation.

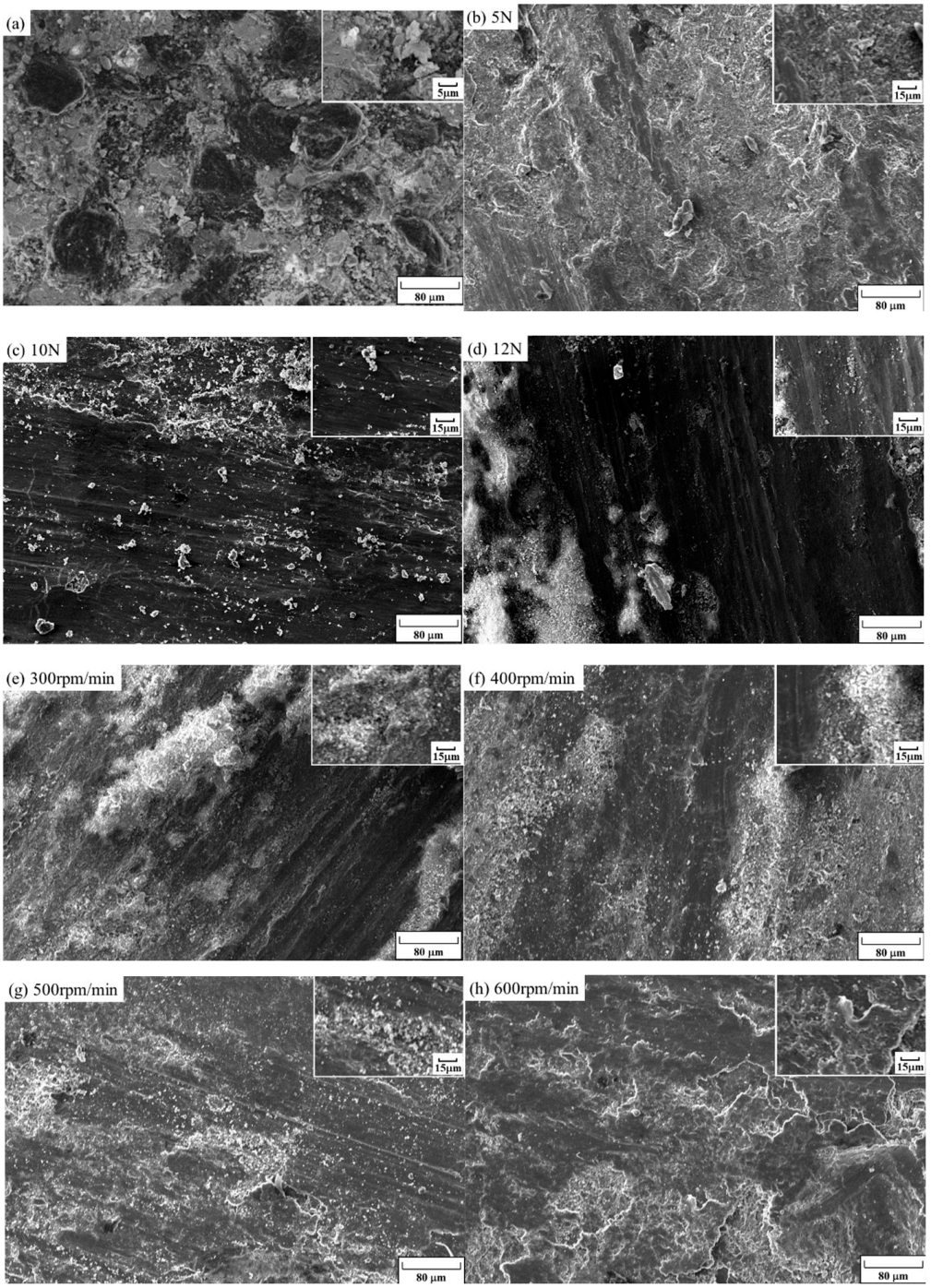


Figure 17. SEM image of wear track of TiC–diamond composites (**a**); Al ball under 5 N (**b**); 10 N (**c**); 12 N (**d**) at 400 rpm/min; under 9.8 N at 300 rpm/min (**e**); 400 rpm/min (**f**); 500 rpm/min (**g**); 600 rpm/min (h).

4. Conclusions

(1) TiC-bonded diamond composites were prepared by HTHP technology, with the main phases produced by a reaction between Ti and C (50 wt.% diamond), resulting in a firmly bonded interface.

(2) The COF of TiC–diamond composites and agate balls increased with load due to adhesive wear, minimizing at 400 rpm/min. The agate ball surface has rough scratches.

(3) POM has a decrease in COF with rotational speed, reaching a minimum at 400 rpm/min under a fixed load of 9.8 N. The wear of TiC–diamond bulks and POM balls decreases with load, while PP balls have pear groove scratches and abrasive debris in the form of flakes. The abrasion scar morphology of PP balls is less effective than that of POM balls under the same friction condition.

(4) Cu and Al balls have less impact on COF due to rotational speed, while the load has a more significant effect on the COF of Cu than that of Al. Adhesive wear is the main friction mechanism of Cu balls, with load increase hardly altering it. TiC–diamond composites with Al balls show increased abrasive wear with increasing load, which is opposite to the effect for adhesive wear.

Supplementary Materials: The following supporting information can be downloaded at: https://www.mdpi.com/article/10.3390/coatings14060735/s1, Figure S1: Optical photographs of POM ball abrasion marks.

Author Contributions: Conceptualization, Y.C. and M.H.; methodology, J.L. and L.L.; data curation, J.L., J.H. and L.L.; writing—original draft preparation, Y.C., J.L. and L.L.; writing—review and editing, Y.C., L.L. and M.H. project administration, J.H.; funding acquisition, Y.C. and M.H. All authors have read and agreed to the published version of the manuscript.

Funding: This research was funded by Science and Technology Open Cooperation Project of Henan Academy of Sciences, grant number 220909003; Youth Fund Project of Natural Science Foundation of Henan Province, grant number 242300421464; Doctoral Special Fund Project of Nanyang Normal College, grant numbers 2024ZX025 and 2019ZX018; and Cultivation Project of National Natural Science Foundation of Nanyang Normal University, grant numbers 2024PY023 and 2023PY011.

Institutional Review Board Statement: Not applicable.

Informed Consent Statement: Not applicable.

Data Availability Statement: The data that support the findings of this study are available on request from the corresponding author, Yuqi Chen, upon reasonable request.

Conflicts of Interest: Author Ming Han was employed by the company Henan Building Materials Research and Design Institute Co., Ltd.,. The remaining authors declare that the research was conducted in the absence of any commercial or financial relationships that could be construed as a potential conflict of interest.

References

1. Yue, Y.; Gao, Y.; Hu, W.; Xu, B.; Wang, J.; Zhang, X.; Zhang, Q.; Wang, Y.; Ge, B.; Yang, Z.; et al. Hierarchically Structured Diamond Composite with Exceptional Toughness. *Nature* **2020**, *582*, 370–374. [CrossRef]
2. Wu, L.; Zhang, G.; Li, B.; Wang, W.; Huang, X.; Chen, Z.; Dong, G.; Zhang, Q.; Yao, J. Study on Microstructure and Tribological Performance of Diamond/Cu Composite Coating Via Supersonic Laser Deposition. *Coatings* **2020**, *10*, 276. [CrossRef]
3. Sokolov, E.; Ozolin, A.; Golius, D. Structure Formation of Diamond–Containing Coatings during Sintering of Specially-Shaped Grinding Wheels. *Coatings* **2022**, *12*, 333. [CrossRef]
4. Zhang, X.; Wang, Y.; Zang, J.; Lu, J.; Zhang, J.; Ge, E.; Cheng, X. Effect of Si Coating on Prevention of Diamond Degradation in Diamond/Glass Composite. *Surf. Coat. Technol.* **2010**, *204*, 2846–2850. [CrossRef]
5. Szutkowska, M.; Jaworska, L.; Boniecki, M.; Stobierski, L.; Rozmus, M. Mechanical Behavior of Diamond Matrix Composites with Ceramic $Ti_3(Si, Ge)C_2$ Bonding Phase. *Int. J. Refract. Met. Hard Mater.* **2015**, *49*, 302–306. [CrossRef]
6. Wan, W.; Wang, J.; Liang, M.; Fan, K.; Wang, Z.; Li, Y. Fracture Behaviors of Ti(C, N) –Based Cermets with Different Contents of Metal Binder. *Ceram. Int.* **2022**, *48*, 32399–32408. [CrossRef]
7. Guignard, J.; Prakasam, M.; Largeteau, A. A Review of Binderless Polycrystalline Diamonds: Focus on the High-Pressure–High-Temperature Sintering Process. *Materials* **2022**, *15*, 2198. [CrossRef]

8. Li, L.; Zhou, A.G.; Wang, L.B.; Hu, F.X. Synthesize Ti_3SiC_2 from TiH_2 by Pressureless Sintering. *Key Eng. Mater.* **2012**, *512–515*, 676–680.
9. Li, Z.; Zhou, A.; Li, L.; Wang, L.; Hu, M.; Li, S.; Gupta, S. Synthesis and Char-acterization of Novel Ti_3SiC_2–cBN Composites. *Diam. Relat. Mater.* **2014**, *43*, 29–33. [CrossRef]
10. Zhou, A.G.; Li, L.; Su, T.C.; Li, S.S. Synthesize Ti_3SiC_2 and Ti_3SiC_2–Diamond Composites at High Pressure and High Temperature. *Key Eng. Mater.* **2012**, *512–515*, 671–675.
11. Li, L.; Zhou, A.; Wang, L.; Li, S.; Wu, D.; Yan, C. In Situ Synthesis of cBN–Ti_3AlC_2 Composites by High-Pressure and High-Temperature Technology. *Diam. Relat. Mater.* **2012**, *29*, 8–12. [CrossRef]
12. Ji, H.; Liang, Y.; Jiang, Z.; Li, Z.; Zhu, Y. Controllable HPHT Sintering and Property of cBN/Diamond Composites Containing Ti_3SiC_2. *Ceram. Int.* **2020**, *46*, 13807–13812. [CrossRef]
13. Lv, X.; Jian, Q.; Li, Z.; Sun, K.; Ji, H.; Zhu, Y. Effect of Controllable Decomposition of MAX Phase (Ti_3SiC_2) on Mechanical Properties of Rapidly Sintered Polycrystalline Diamond by HPHT. *Ceram. Int.* **2019**, *45*, 16564–16568. [CrossRef]
14. Jiang, Z.; Jian, Q.; Han, Y.; Zhu, Y.; Li, Z. Performance Evaluation of cBN-Ti_3AlC_2–Al Composites Fabricated by Hthp Method. *Ceram. Int.* **2020**, *46*, 24449–24453. [CrossRef]
15. Sun, F.; Huang, L.; Zhang, R.; Wang, S.; Jiang, S.; Sun, Y.; An, Q.; Jiao, Y.; Geng, L. In-Situ Synthesis and Superhigh Modulus of Network Structured TiC/Ti Composites Based on Diamond-Ti System. *J. Alloy Compd.* **2020**, *834*, 155248. [CrossRef]
16. Bhaumik, S.; Divakar, C.; Singh, A.; Upadhyaya, G. Synthesis and Sintering of TiB_2 and TiB_2–TiC Composite under High Pressure. *Mater. Sci. Eng. A* **2000**, *279*, 275–281. [CrossRef]
17. Li, L.; Chen, Y. The Influence of Sintering Pressure on the Preparation, Friction Properties, and Magnetic Properties of Ti_2AlC–TiC and Ti_3AlC_2–Tic Composites under High-Pressure and High-Temperature. *Adv. Mater. Sci. Eng.* **2022**, *2022*, 1–12. [CrossRef]
18. Chen, Y.; Liang, L.; Ma, S.; Chao, L.; Zheng, S.; Lv, W.; Wang, L.; Zhou, A.; Xing, W. Preparation of $Ti_3Si_{0.8}Al_{0.2}C_2$ Bonded Diamond Composites and Their Friction Properties Coupled with Different Counterfaces. *Adv. Mater. Sci. Eng.* **2023**, *2023*, 1–14. [CrossRef]
19. Qin, J.; He, D. Phase stability of Ti_3SiC_2 at High Pressure and High Temperature. *Ceram. Int.* **2013**, *39*, 9361–9367. [CrossRef]
20. Li, X.; Xu, L.; Chen, Q.; Cao, X.; Liu, L.; Wang, Y.; Zhang, H.; Meng, C.; Wu, Q. Investigation of Formation Mechanism of Ti_3SiC_2 by High Pressure and High-Temperature Synthesis. *High Press. Res.* **2018**, *38*, 440–447. [CrossRef]
21. Garcia, C.; Smith, J.D.; Rodriguez, J.; DiGiovanni, A.A.; Scharf, T.W. Reactive Spark Plasma Sintering of SiC–TiC–Diamond Composites. *Diam. Relat. Mater.* **2022**, *129*, 109384. [CrossRef]
22. Anna, D.; Koczorowski, W.; Trzcinski, M.; Mosińska, L.; Szybowicz, M. The Effect of Surface Treatment on Structural Properties of CVD Diamond Layers with Different Grain Sizes Studied by Raman Spec-troscopy. *Materials* **2021**, *14*, 1301.
23. Yang, L.; Jiang, C.; Guo, S.; Zhang, L.; Gao, J.; Peng, J.; Hu, T.; Wang, L. Novel Diamond Films Synthesis Strategy: Methanol and Argon Atmosphere by Microwave Plasma CVD Method Without Hydrogen. *Nanoscale Res. Lett.* **2016**, *11*, 1–6. [CrossRef] [PubMed]
24. Maria, I.; Ovodok, E.; Kotsikau, D.; Azarko, I.; Micusik, M.; Omastova, M.; Golovanov, V. Structural Transformation and Nature of Defects in Titanium Carbide Treated in Different Redox Atmospheres. *RSC Adv.* **2020**, *10*, 25602–25608.
25. Gong, Y.; Tu, R.; Goto, T. High-Speed Deposition of Titanium Carbide Coatings by Laser-Assisted Metal–Organic CVD. *Mater. Res. Bull.* **2013**, *48*, 2766–2770. [CrossRef]
26. Anna, I.; Song, C.; Zhu, W.; Zhang, J.; Bauer, A.; Baker, R.; Neburchilov, V.; Ye, S.; Campbell, S. Titanium Carbide and Its Core-Shelled Derivative TiC@TiO_2 as Catalyst Supports for Proton Exchange Membrane Fuel Cells. *Electrochim. Acta* **2012**, *69*, 397–405.
27. Guo, Y.; Gao, Y.; Chen, H.; Zhao, Q.; Zhu, Q.; Cao, Z.; Li, B.; Shang, J.; Du, Z.; Yang, S. Controllable Etching of Ti_3SiC_2 to Produce Fluorine-Enriched, Hydrophobic 2D Titanium Carbide for Ultrastable Zinc Ion Batteries. *Adv. Energy Mater.* **2023**, *13*, 2300890. [CrossRef]
28. Zhang, R.; Feng, W.; Liu, F. Tribo-Oxide Competition and Oxide Layer Formation of Ti_3SiC_2/CaF_2 Self-Lubricating Composites During the Friction Process in a Wide Temperature Range. *Materials* **2021**, *14*, 7466. [CrossRef] [PubMed]
29. Olha, M.; Michael, N.; Yury, G.; Thierry, D. Anodized Ti_3SiC_2 as an Anode Material for Li–Ion Microbatteries. *ACS Appl. Mater. Interfaces* **2016**, *8*, 16670–16676.
30. Zhu, Y.; Zhou, A.; Ji, Y.; Jia, J.; Wang, L.; Wu, B.; Zan, Q. Tribological Properties of Ti_3sic_2 Coupled with Different Counterfaces. *Ceram. Int.* **2015**, *41*, 6950–6955. [CrossRef]
31. Thomas, E.L.; Nelson, G.W.; Mandal, S.; Foord, J.S.; Williams, O.A. Chemical Mechanical Polishing of Thin Film Diamond. *Carbon* **2014**, *68*, 473–479. [CrossRef]
32. Xiong, X.; Hua, L.; Wan, X.; Yang, C.; Xie, C.; He, D. Experiment and Simulation of Friction Coefficient of Polyoxymethylene. *Ind. Lubr. Tribol.* **2018**, *70*, 273–281. [CrossRef]
33. Sun, L.H.; Yang, Z.-G.; Li, X.-H. Study on the Friction and Wear Behavior of POM/Al_2O_3 Nanocomposites. *Wear* **2008**, *264*, 693–700. [CrossRef]
34. Chen, Y.; Lin, Y. A Calculation Method for Friction Coefficient and Meshing Efficiency of Plastic Line Gear Pair under Dry Friction Conditions. *Friction* **2021**, *9*, 1420–1435. [CrossRef]
35. Omrani, E.; Menezes, P.L.; Rohatgi, P.K. State of the Art on Tribological Behavior of Polymer Matrix Composites Reinforced with Natural Fibers in The Green Materials World. *Eng. Sci. Technol. Int. J.* **2016**, *19*, 717–736. [CrossRef]

36. Lebedev, O.V.; Bogdanova, O.I.; Goncharuk, G.P.; Ozerin, A.N. Tribological and Percolation Properties of Polypropylene/Nanodiamond Soot Composites. *Polym. Polym. Compos.* **2020**, *28*, 369–377. [CrossRef]
37. Orozco, V.H.; Vargas, A.F.; Brostow, W.; Datashvili, T.; López, B.L.; Mei, K.; Su, L. Tribological Properties of Polypropylene Composites with Carbon Nanotubes and Sepiolite. *J. Nanosci. Nanotechnol.* **2014**, *14*, 4918–4929. [CrossRef] [PubMed]

Disclaimer/Publisher's Note: The statements, opinions and data contained in all publications are solely those of the individual author(s) and contributor(s) and not of MDPI and/or the editor(s). MDPI and/or the editor(s) disclaim responsibility for any injury to people or property resulting from any ideas, methods, instructions or products referred to in the content.